ACCSCIENCE PUBLISHING

Materials Science in Additive Manufacturing

ORIGINAL RESEARCH ARTICLE

Numerical simulation and experimental characterization of a single-seam plasma wire arc additive manufacturing process for Ti-6Al-4V

Martin Bielik [1,2*], Erich Neubauer [2], Michael Kitzmantel [2], Ingo Neubauer [3], and Ernst Kozeschnik [1]

[1]Institute of Materials Science and Technology, Faculty for Mechanical and Industrial Engineering, Vienna University of Technology, Vienna, Austria

[2]RHP-Technology GmbH, RHP Group, Research and Technology Center, Seibersdorf, Lower Austria, Austria

[3]Division of Manufacturing Intelligence, Hexagon GmbH, Hamburg, Germany

Abstract

Arc welding processes are increasingly being used in the additive manufacturing of metal components. Physics-based modeling of welding processes enables the study of welding parameter effects on the final weld shape, residual stress state, and distortion, helping to improve weld quality and reduce costs. However, the quality of the process simulation strongly depends on the mathematical description of the heat source. The parameters of the heat source model have a significant influence on the temperature field and, consequently, on the distortion and residual stress fields. This paper presents a trial-and-error method for determining the parameters for Goldak's double-ellipsoidal heat source model. The transient temperature distribution and the size of the melt pool are determined through experimental studies. Numerical models are then set up in Simufact Welding 8.0 with a set of heat source parameters to reproduce the experimental trials. By comparing numerical finite element results with experimental results, the heat source parameters for a multi-pass additive manufacturing process are successfully calibrated and identified.

Keywords: Wire arc additive manufacturing; Finite element method; Heat source model; Melt pool; Ti6Al4V

***Corresponding author:**
Martin Bielik
(martin.bielik@gmx.at)

Citation: Bielik M, Neubauer E, Kitzmantel M, Neubauer I, Kozeschnik E. Numerical simulation and experimental characterization of a single-seam plasma wire arc additive manufacturing process for Ti-6Al-4V. *Mater Sci Add Manuf.* 2025;4(3):025140021
doi: 10.36922/MSAM025140021

Received: April 3, 2025

Revised: April 30, 2025

Accepted: May 2, 2025

Published online: June 17, 2025

Copyright: © 2025 Author(s). This is an Open-Access article distributed under the terms of the Creative Commons Attribution License, permitting distribution, and reproduction in any medium, provided the original work is properly cited.

Publisher's Note: AccScience Publishing remains neutral with regard to jurisdictional claims in published maps and institutional affiliations.

1. Introduction

Additive manufacturing (AM) is one of the most innovative and transformative manufacturing processes. According to the International Organization for Standardization/American Society for Testing and Materials 52900, wire arc additive manufacturing (WAAM) is classified as a directed energy deposition process, in which focused thermal energy is used to fuse materials by melting them as they are deposited.[1] Among various AM technologies, WAAM stands out as a novel approach that enables high deposition rates and facilitates the production of large, near-net-shape components at relatively low process costs. In addition, WAAM offers a high buy-to-fly ratio, making it particularly advantageous for aerospace and other high-performance applications.[2-4]

Various arc processes can be used as the energy source in WAAM, including gas metal arc welding, gas tungsten arc welding, and plasma arc welding.[5] A defining characteristic of these welding processes is the localized heat input from a moving high-energy-density heat source, which leads to the formation of transient temperature fields in the material. The evolution of the temperature fields is influenced by the thermo-physical properties of the material, the path strategy, and welding parameters.[6]

Because WAAM is a multi-layer welding process in which the feedstock material is melted and deposited in layers, the previously deposited near-net-shape structure is repeatedly remelted and reheated with each new layer. The cyclic thermal exposure induces non-uniform thermal expansion in both the deposited material and the surrounding base material, leading to the formation of residual stresses and distortion fields.[7] The deformation and residual stresses of WAAM-produced components, particularly those made from titanium and steel, have been studied extensively.[8-11] Residual stresses influence several critical failure mechanisms, including fracture and fatigue properties, stress corrosion cracking, and distortion.[12]

The complex thermal history of parts produced with WAAM poses significant challenges in predicting residual stresses and distortion fields. As a result, numerical process simulation has emerged as a feasible and cost-effective method for predicting temperature distributions, distortions, and stress fields in the parts during the printing process.[13,14] However, the quality of the process simulation strongly depends on the mathematical description of the heat source. The configuration of the heat source, including parameter adjustments and thermal conductivity settings, plays a critical role in determining the accuracy of simulated results, particularly in predicting distortions and residual stresses.[15]

In this study, a trial-and-error approach is used to calibrate the numerical heat source by iteratively adjusting parameters until the simulated temperature fields match the experimental data.[16] Since these parameters are highly dependent on the welding conditions, their accurate determination requires the solution of an inverse optimization problem through appropriate experiments.[17] The calibration process involves refining multiple parameters to achieve a validated temperature field, ensuring consistency with thermal cycles recorded by thermocouples and the weld pool geometry observed in light-optical micrographs.[18] Several variants of Goldak's double-ellipsoid heat source model[19] are tested and compared within Simufact Welding 8.0, allowing for a systematic validation of the numerical model.

2. Materials and methods

2.1. Heat source model

In the arc welding module of Simufact Welding 8.0, the Goldak double-ellipsoid model is implemented as the default heat source (Figure 1). This moving double-ellipsoid model is widely used to simulate various arc welding techniques, including gas metal arc welding, gas tungsten arc welding, shielded metal arc welding, and submerged arc welding.[20]

The thermal analysis of the WAAM process involves solving a heat transfer problem with a moving heat source. The heat source mathematically describes the heat transfer from the arc to the melt pool, characterizing the energy distribution within the weld pool. The goal of this model is to approximate the isothermal surface of the actual melt pool and the heat flow across that surface with high accuracy. The effects of the melt pool are considered indirectly.

The Goldak model describes a Gaussian distributed heat generation per unit volume defined in a moving reference frame. A local Cartesian coordinate system (x, y, and z) is defined at the weld point with the x-axis aligned with the welding direction and the z-axis perpendicular to the welding torch. The heat source moves at a constant velocity v along the x-axis.

To account for the asymmetric nature of the heat distribution in the melt pool, two power distribution functions q_f and q_r (W/m³) are used for the front and rear semi-ellipsoidal regions, respectively.[19] The power density distribution is defined in Equation I:

$$q(x,y,z,t)=\frac{6\sqrt{3}Q}{\pi\sqrt{\pi}bd}\begin{cases}\dfrac{f_{\mathrm{f}}}{a_{\mathrm{f}}}\cdot\exp\left[-\dfrac{3(x-vt)^2}{a_{\mathrm{f}}^2}-\dfrac{3y^2}{b^2}-\dfrac{3z^2}{d^2}\right] & \text{for } x>vt\\ \dfrac{f_{\mathrm{r}}}{a_{\mathrm{r}}}\cdot\exp\left[-\dfrac{3(x-vt)^2}{a_{\mathrm{r}}^2}-\dfrac{3y^2}{b^2}-\dfrac{3z^2}{d^2}\right] & \text{for } x<vt\end{cases} \quad (I)$$

Where Q is the total power (W), a_f and a_r are the front and rear ellipsoid lengths (m), b is the ellipsoid width (m), d is the ellipsoid depth (m), and f_f and f_r are the fractions of heat distributed in the front and rear ellipsoids, respectively. The front and rear fractions satisfy the condition $f_f + f_r = 2$ to ensure continuity of the volumetric heat source. Goldak *et al.*[19] suggest default values that set the front fraction to $f_r = 0.6$ if experimental data are insufficient. These fractions can be computed automatically when the geometric parameters are known (Equation II).[21,22]

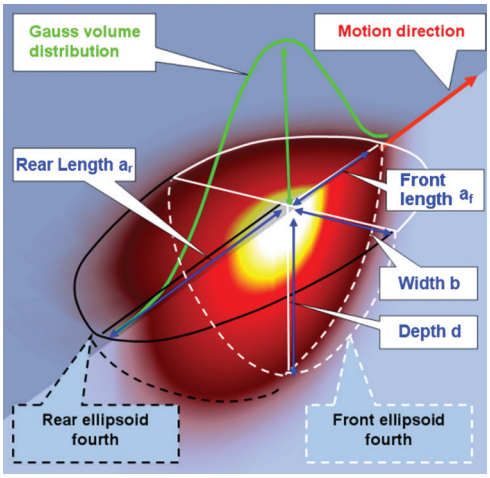

Figure 1. Illustration of Goldak's double-ellipsoid heat source model. Reprinted with permission from Hexagon Manufacturing Intelligence GmbH, Simufact Infosheet Heat Source[20].

$$f_f = 2\frac{a_f}{a_f + a_r}, f_r = 2\frac{a_r}{a_f + a_r} \quad \text{(II)}$$

The heat input during welding plays a critical role in determining the thermal cycles and the properties of the weld. For arc welding, the power input Q (J) by the torch is given in Equation III,

$$Q = \eta\, UI \quad \text{(III)}$$

where I is the current (A), U is the voltage (V), and η is the thermal efficiency (-), linking the gross and net heat inputs.

To calibrate the Goldak double-ellipsoid heat source model, six key parameters must be determined: a_f, a_r, b, d, M, and η. The front length a_f, the rear length a_r, the width b, and the depth d are geometric parameters that define the fusion and heat-affected zone (HAZ). These parameters can be obtained from micrographs of cross-sections of the weld pool shape or *in situ* measurements of the weld pool. The Gaussian parameter M controls the width of the Gaussian bell curve, which affects the energy density over the weld area. The thermal efficiency η defines the fraction of the input energy that is effectively transferred to the workpiece.

Accurate calibration of the double-ellipsoid heat source model is essential for achieving realistic simulation results. The process involves iterative adjustments to fit numerical predictions to experimental data, minimizing discrepancies between simulated and measured temperature fields. However, inherent measurement uncertainties can introduce errors in the calibration process that affect the accuracy of the model.

2.1.1. Governing equations

Finite element (FE) simulations are conducted to compute transient temperature fields, which subsequently serve as input for a thermal elasticplastic mechanical analysis to evaluate deformations and residual stresses of large-scale Ti6Al4V WAAM components. Welding simulations are typically performed as sequential coupled analyses, where the transient temperature field is first computed, followed by structural mechanics calculations. Consequently, the AM process is divided into two primary stages: A heat transfer analysis and a mechanical analysis. These stages are computed separately in a one-way thermo-mechanical coupling approach, meaning that the transient thermal distributions recorded during material deposition are stored at specific time steps and then used as input data for the mechanical analysis.[23] The calibration of the heat source was performed solely based on thermal computations. Therefore, only the governing equations for the thermal model are presented in this study. A complete analysis of the WAAM process requires a fully coupled thermo-mechanical model.

To accurately model the thermal effects of the WAAM process, the total heat input into the component must be determined. The heat flow is derived from the process parameters, considering thermal efficiency and the plasma arc's density distribution function. The thermal behavior is governed by the energy balance equation, which controls temperature evolution and solidification. This equation describes the temporal distribution of heat in a solid medium, incorporating temperature-dependent material properties, and can be expressed as a function of temperature[24] in Equation IV,

$$\frac{\partial T}{\partial t} = \frac{\lambda(T)}{\rho(T)c_p(T)}\vec{\nabla}^2 T + \frac{1}{\rho(T)c_p(T)}\frac{\partial Q_V(x,y,z,t)}{\partial t} \text{ with } T = T(x,y,z,t) \quad \text{(IV)}$$

Where λ is the heat conductivity (W/[m·K]), ρ is the density (kg/m³), c_p is the specific heat capacity (J/[kg·K]), T is the temperature (K), and Q_v is the volumetric heat source (J). The temperature and volumetric heat source are functions of time and spatial coordinates. The general solution of the temperature distribution is obtained by applying the following boundary and initial conditions, which can be written as Equation V.

$$\dot{\vec{q}}_S = -\lambda(T)\frac{\partial T}{\partial \vec{n}}\Big|_S = -\lambda(T)\vec{\nabla}T\Big|_S \quad \text{(V)}$$

$$T(x, y, z, t = 0) = T_0(x, y, z)\big|_{t=0}$$

The heat flux per unit of surface q_s (W/[m²·K]) is computed using Fourier's law. According to Fourier's law, the rate of heat transfer through a material is proportional to the negative temperature gradient and the area through which the heat flows. Heat transfer continues as long as a temperature gradient is present. The proportionality constant λ depends on factors, such as chemical composition, microstructure, and temperature.

Thermal boundary conditions applied on the surface of the computational domain can be described as a Dirichlet (temperature history), Neumann (heat flux history), or Robin boundary condition, which represents a combination of both. In WAAM, the primary heat transfer mechanisms include conduction and surface heat losses, both of which vary depending on the location within the component. In the first layers, the cold baseplate acts as a heat sink, making conduction the dominant heat transfer mechanism. However, as the deposition progresses, the increasing substrate temperature and wall height lead to a greater influence of convective and radiative heat transfer.

Heat radiation is the transfer of internal energy in the form of electromagnetic waves, governed by the Stefan–Boltzmann law, which describes the heat flow rate emitted or absorbed by an object as a function of its temperature. This law applies to all free surfaces, including those of the newly deposited material, and represents the Neumann component of Equation V, as in Equation VI,

$$q_{\mathrm{R}} = \epsilon \sigma \left(T_{\mathrm{S}}^4 - T_{\infty}^4 \right) \tag{VI}$$

where ε is the emissivity (-), σ is the Stefan–Boltzmann constant (W/[m²·K⁴]), T_s is the surface temperature, and T_∞ is the far field temperature. The emissivity can be determined experimentally and numerically as an inverse problem. If the emissivity is known, the temperature of a body can be determined from the heat radiation emitted by the body. However, the emissivity is not only material-dependent but is also influenced by surface conditions of the body, such as oxidation.

Heat convection is a mode of heat transfer driven by the mass motion of a fluid. The movement of a fluid can be forced (forced convection) or free (natural convection). The governing equation of heat convection is Newton's law, expressed as in Equation VII,

$$q_c = h_c \left(T_s - T_\infty \right) \tag{VII}$$

where h_c is the convective heat transfer coefficient in W/(m²·K). The coefficient depends on the type of media (gas or fluid), flow conditions on the surface, surface properties, and temperature, and is typically determined using empirical formulas based on dimensionless parameters.

In addition to radiation and convection, heat transfer between bodies in contact affects thermal behavior. Heat transfer at an interface depends on the temperature of the contacting bodies and the contact heat transfer coefficient a (W/[m²·K]) in Equation VIII.

$$q_a = a \left(T_1 - T_2 \right) \tag{VIII}$$

Due to manufacturing limitations, technically, processed surfaces are not perfectly smooth, and microscopic surface roughness leads to small media-filled gaps at the interface. Consequently, heat transfer across the contact interface occurs through two mechanisms. First, solid-to-solid conduction at points where contact is established, and second, media conduction through the air- or gas-filled gaps. The contact heat transfer coefficient a depends on the materials in contact, the surface conditions of the contacting bodies, contact pressure, and the fluid inside the cavities.

Thermal boundary conditions are modeled by integrating Equations VI to VIII into Equation V, as Equation IX

$$\epsilon \sigma \left(T_{\mathrm{S}}^4 - T_{\infty}^4 \right) + h_{\mathrm{c}} \left(T_{\mathrm{S}} - T_{\infty} \right) + a \left(T_1 - T_2 \right) = -\lambda \vec{\nabla} T \tag{IX}$$

Since the cooling behavior of the model is governed by heat transfer at the boundaries, inaccuracies in defining these mechanisms can significantly impact the simulation results.[25]

2.1.2. Thermal material properties

Structural welding simulations require the specification of temperature-dependent Thermo-physical and thermo-mechanical material parameters. Thermo-physical parameters include thermodynamic quantities, such as thermal conductivity, density, and heat capacity, as well as thermo-metallurgical parameters that characterize solid phase transformations. Thermo-mechanical properties encompass material characteristics, such as thermal expansion, modulus of elasticity, transverse contraction, stress-strain behavior, and transformation plasticity. These parameters are determined experimentally or sourced from literature and material databases, such as JMatPro. Simufact Welding includes an integrated material database that provides relevant parameters for conducting structural welding simulations.

2.2. Experimental setup

Deposition experiments were performed using a custombuilt WAAM system at RHPTechnology GmbH, Austria. The system utilizes plasma metal deposition, a process that uses a plasmatransferred arc energy source in combination with wire feeding to produce three-dimensional parts (Figure 2A). The

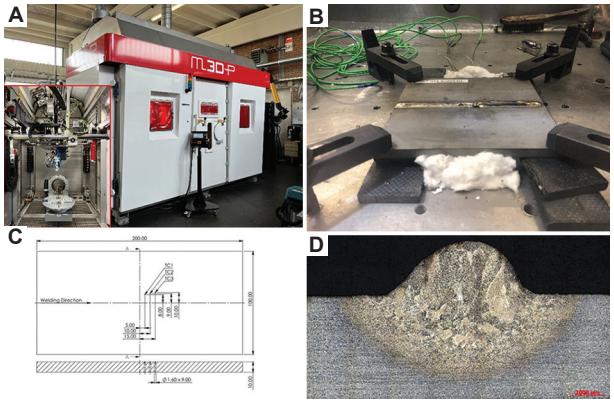

Figure 2. Experimental setup for the heat source calibration. (A) M3DP welding system. (B) Experimental setup for the calibration runs. (C) Thermocouple locations. (D) Micrograph after single bead deposition. Scale bar: 2,000 µm, magnification 5×

deposition process took place within a closed, airtight welding chamber filled with highpurity argon, providing an inert gas atmosphere for adequate shielding. Weldinggrade argon (99.99% purity) was used in both the process and as a shielding gas. Cold Ti6Al4V wire with a diameter of 1.2 mm was continuously fed by an automatic wire feeder. Both base plates and welding wire are commercially available and conform to the American Society for Testing and Materials B265 and American Welding Society A5.16 - 07 standards, respectively.

The experimental setup for the heat source calibration is shown in Figure 2B. To minimize heat loss, the baseplate was supported with carbon fiber composites, and the air gap between the baseplate and the backing plate was filled with alumina wool, which effectively isolated the bottom surface of the baseplate. This design reduced contact heat transfer to the backing plate as well as convective heat loss through the air gap. Weld beads 170 mm in length are deposited to establish a steady thermal process.

To characterize the thermal profiles within the workpiece, thermocouples were positioned at pre-defined measurement locations on the baseplate (Figure 2C), following the methodology described by P. Helbig.[26] These thermocouples recorded peak temperatures and thermal gradients within the workpiece. Insulated type K thermocouples were inserted from the bottom of the baseplate into pre-drilled holes, with direct thermal contact provided by the application of a thermally conductive paste. Temperature was recorded using a PCET 390multi-channel digital thermometer (PCE Instruments GmbH, Germany) with a sampling rate of 1 Hz. In total, three calibration runs were performed: a single pre-heating pass, a single printing pass, and two pre-heating passes with a subsequent printing pass.

To improve adhesion and optimize bead geometry, pre-heating of the baseplate was applied as a process control measure. This strategy effectively reduced thermal stress, minimized cracking, and promoted a more uniform temperature distribution.[27] By increasing the initial temperature of the baseplate, pre-heating prevented the first deposited track from becoming excessively narrow, promoted better metal spreading, and improved metallurgical bonding between the deposited material and the baseplate. Beyond thermal management, pre-heating the baseplate significantly influenced the microstructural evolution of Ti6Al4V in the WAAM process. The first layers experienced relatively high cooling rates due to rapid heat conduction into the cold baseplate, resulting in steeper thermal gradients.[28] Elevated pre-heat temperatures reduced these thermal gradients, slowing cooling rates and consequently modifying the solidification behavior and phase transformation kinetics. According to Tan *et al.*,[29] pre-heating of the baseplate contributed to melt pool stabilization, affected grain growth dynamics, and facilitated microstructural homogenization. These effects are crucial for reducing columnar grain formation, improving part integrity, and enhancing the overall mechanical properties of WAAM-produced components.

The most critical process parameters are the welding current I, the travel speed of the plasma torch, and the wire feed speed, influencing the deposited metal shape.[29] The specific deposition parameters used in the experiments are shown in Table 1.

After the experiments, samples were extracted along the sectional plane A-A (Figure 2C), embedded in bakelite, ground, polished, and etched with Kroll's agent. Metallographic analysis was performed using an optical microscope (Zeiss, Germany) to evaluate the microstructure and measure the dimensions of the weld and HAZ. An example micrograph of single bead deposition is shown in Figure 2D. From these micrographs, the width b, depth d, and cross-sectional area A of the weld bead and HAZ were determined. In this context, the depth d represents the height of the weld seam.

2.3. *FE model*

Wire arc AM can be analyzed at different scales: macro, meso, and micro.[30] At the macro-scale, multi-purpose FE software (Simufact Welding 8.0) was used to simulate the coupled thermo-mechanical behavior of WAAM parts, where a generic heat source model replaces the welding torch and electric arc.

Within Simufact Welding 8.0, the welding process was modeled based on key manufacturing parameters, including the welding process, energy input, welding speed, filler material, metallurgical properties, clamping concept, components of interest, and the FE mesh configuration.

All components were initially designed in SolidWorks 2020 and then meshed in Abaqus CAE 6.14. To optimize computational efficiency, the symmetry properties were exploited by modeling only half of the calibration setup.

To simplify the simulation and facilitate the efficient implementation of thermal interactions, the carbon fiber composites support and the alumina wool insulation were modeled as a single component. This allowed a single effective contact heat transfer coefficient to be applied to the underside of the baseplate. The cross-section profiles of the weld beads were approximated by a second-degree polynomial fitting, expressed as Equation X.

$$f(x) = c_2 x^2 + c_0 \quad \text{(X)}$$

The parabolic representation closely approximates the actual shape of the weld beads, ensuring geometric consistency between the numerical model and the experimental observations. The FE model of the calibration setup is shown in Figure 3.

Figure 3A shows the three-dimensional half-symmetry FE mesh used for the thermal analysis of the calibration experiments. To ensure accurate thermal behavior near the heat source, a refined mesh was applied to the weld bead and surrounding region along the welding line, with element sizes of 1 × 0.5 × 0.5 mm. The mesh became progressively coarser along the *y*-axis, moving away from the weld line (Figure 3B). A total simulation time of 400 s

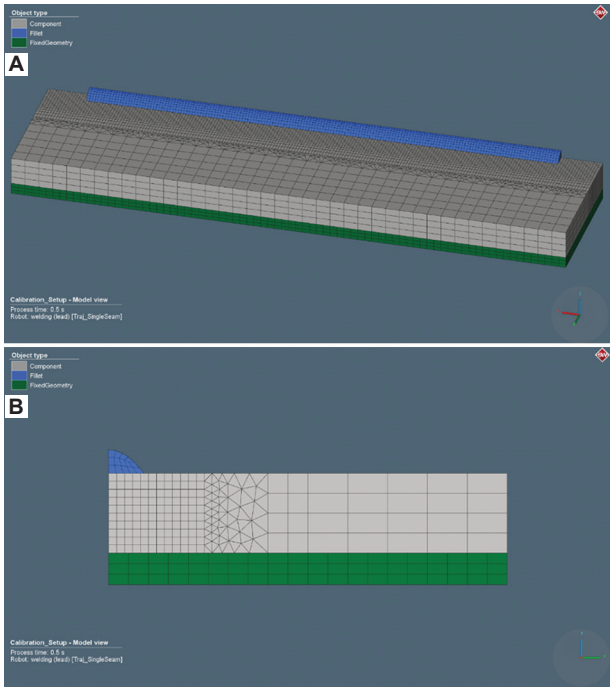

Figure 3. Three-dimensional half-symmetry finite element model. (A) Model view of the calibration setup. (B) Crosssection view of the calibration model.

was set to accurately capture the cooling behavior of the assembly and to precisely define the heat source parameters and cooling parameters.

The moving heat source was calibrated using an iterative trial-and-error approach, where the simulation's fusion zone shape and temperature profiles were matched against experimental results by adjusting the heat source's geometric parameters and thermal boundary conditions.

The melt pool dimensions obtained from the metallurgical analysis were used to define the geometric parameters of the Goldak double-ellipsoid heat source. The width *b* and depth *d* of the fusion zone were measured directly from the micrographs of the weld pool cross-sections. The front and rear ellipsoid lengths, a_f and a_r, were estimated based on the empirical relationships provided by Simufact[20] using Equation XI.

$$a_f = b$$
$$a_r = 2b \quad \text{(XI)}$$

In addition to defining the heat source parameters, thermal boundary conditions were incorporated to simulate the cooling behavior of the component. These included the convective heat transfer coefficient *h*, the contact heat transfer coefficient *a*, and the radiative heat transfer *ε*. The thermal boundary conditions were fine-tuned through an iterative trial-and-error calibration process to ensure that the simulated cooling behavior matched experimental observations.

3. Results

3.1. Weld bead analysis

The shape of the weld bead and its adhesion to the baseplate are critical factors influencing the mechanical performance and structural integrity of welded components. In WAAM, achieving a stable and well-bonded weld bead is essential for ensuring high-quality deposition and minimizing defects. The interaction between the molten metal and the baseplate is governed by the wetting behavior, which is characterized by the wetting angle at the interface of the solid, liquid, and vapor phases. The presence of solid–liquid–vapor interfaces and related interfacial phenomena plays an extremely important role in high-temperature processes, such as welding. A well-attached weld bead exhibits a favorable wetting angle, promoting strong bonding and reducing the risk of defects, such as undercuts, lack of fusion, or delamination from the baseplate.

The deposition of molten metal in WAAM occurs through the formation of liquid metal droplets at the interface between the baseplate and the fed wire. The shape

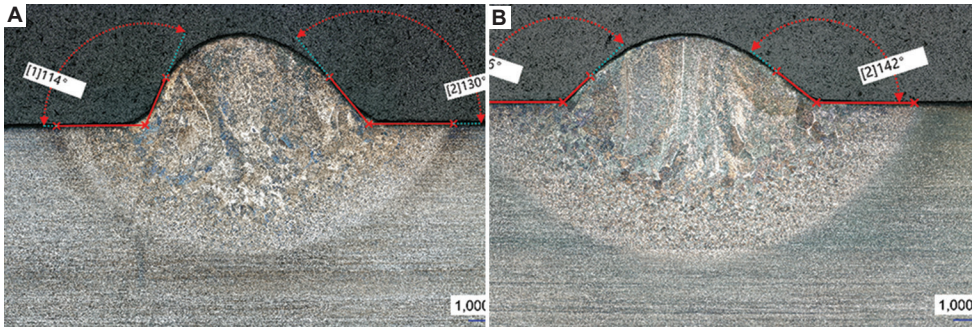

Figure 4. Complementary wetting angles. (A) Single bead. (B) Single bead with two preceding pre-heating passes. Scale bar: 1,000 µm, magnification 5×

and stability of these droplets are governed by process parameters and the interplay between volumetric forces, such as gravity and electromagnetic forces, and interfacial phenomena, such as surface tension and drag forces.[31] These factors, in combination with heat and mass transfer mechanisms, dictate the formation of the weld pool and ultimately influence the overall quality of the welding process. To assess the effects of the wetting behavior of the molten metal on the baseplate, the wetting angles of both the printing pass and the printing pass with pre-heating are analyzed (Figure 4).

The corresponding wetting angles of the left θ_{left} and right θ_{right} side are shown in Table 2.

Asymmetries between the left and right sides of the deposited beads resulted from the transverse feeding direction of the wire. During deposition, the molten droplets are pushed outward on the side opposite to the wire feed direction, leading to steeper wetting angles. Moreover, pre-heating has been observed to reduce wetting angles, thereby enhancing the wettability of the molten material on the baseplate. The formation of various weld-shape defects, such as undercuts (wetting angles exceeding 90°), lack of fusion, and lack of penetration, is closely linked to the wettability of the solid metal by the molten metal.[31] Furthermore, the shape of the deposited bead and the minimum achievable thickness of the deposited material are directly influenced by the wetting angle. Based on these findings, it can be depicted that pre-heating the baseplate, whether by hot plasma gas or heating mats, has a beneficial impact on interlayer bonding, improving the adhesion between the first deposited layer and the baseplate.

3.2. Heat source calibration

The moving heat source is calibrated by fitting the simulated fusion zone and temperature profiles to experimental data through an iterative adjustment of the heat source's geometric parameters and thermal boundary conditions. The calibration process ensures that the prescribed heat input accurately reflects the physical power distribution of the welding arc. Since the heat input directly affects the accuracy of the WAAM process simulations, accurate calibration is essential. The parameters of the Goldak double-ellipsoid heat source for both pre-heating and printing were determined by trial-and-error analysis, as summarized in Table 3.

Cooling behavior and arc efficiency were determined by inverse simulation, ensuring agreement with experimental

Table 1. Deposition parameters

Description	Symbol	Preheating	Deposition	Unit
Wire diameter	d	-	1.2	mm
Welding current	I	130	140	A
Voltage	U	25	25	V
Travel speed	v_{TS}	300	200	mm/min
Feed rate	f	-	0.9	kg/h
Wire feed speed	v_{WFS}	-	2,910	mm/min
Cooling time	t_{cool}	1	30	s
Total dwell time	t_{dwell}	9	38	s
Number of layers	N	2	32	-
Pilot gas		1.5	1.5	l/min
Shielding gas		5	5	l/min

Table 2. Wetting angles

Calibration	θ_{left} (°)	θ_{right} (°)
Single bead	66	50
Single bead plus pre-heating	44	38

Table 3. Goldak double-ellipsoid heat source parameters obtained by trial-and-error

Run	a_f (mm)	a_r (mm)	b (mm)	d (mm)	M (-)	f_f (-)
Preheating	2.85	5.70	2.85	1.4	0	0.66
Deposition	6.72	13.44	6.72	4.41	0	0.66

observations. The final values give an arc efficiency of 0.4, an emissivity of 0.7, a convective heat transfer coefficient of 8 W/(m²·K), and a contact heat transfer coefficient of 10 W/(m²·K). These parameters are assumed to be temperature-independent throughout the simulation.

3.2.1. Double-ellipsoid heat source validation

Accurate modeling of the heat source is critical for realistic simulations of welding processes. The calibration process ensures that the simulated weld pool dimensions match the experimental measurements. During calibration, key parameters such as weld penetration and weld width were systematically fine-tuned to achieve the best agreement with experimental results. A visual comparison of experimental and simulated weld profiles is shown in Figure 5.

The fusion zone boundary in the simulation is defined by the solidification temperature of Ti6Al4V, which is 1,550°C. As shown in Figure 5A, the experimental fusion zone of the single bead is closely reproduced, although the simulated penetration depth is slightly underestimated. However, for the pre-heating pass (Figure 5B), the simulation overestimated the weld pool size compared to the experimental measurements. One possible explanation is the omission of melt pool flow effects in the simulation that affect heat dissipation and melt zone morphology, leading to numerical predictions that are different from those experimentally measured. Visual assessment of the micrograph in Figure 5B reveals that the liquid metal is drawn downward in the peripheral areas while being forced upward toward the center. In contrast, the numerical model for pre-heating does not account for any weld pool geometry; instead, the pre-heating pass is represented as a flat surface, as no wire feedstock is deposited. In addition, arc pressure, which exerts a force on the melt pool, influences the weld pool shape by directing the flow of liquid metal. Thus, melt pool dynamics play a crucial role in the melting process, influencing the weld pool geometry, heat flow, temperature, and temperature gradients.[32] In Figure 5C, the simulation overestimates the penetration depth of the weld pool. This effect is attributed to the larger-than-expected pre-heating fusion zone, which delivers excess energy to the baseplate, causing deeper penetration than experimentally observed.

The ratio of melt width to melt depth $\phi = 2b/d$ is an indicator of the evolution of the weld pool geometry, with higher values corresponding to wider and shallower pools.

Experimental melt pool aspect ratios from Table 4 show that pre-heating results have significantly larger ratios than single beads. Unlike single beads, pre-heating does not involve feedstock material deposition, and melt pool dynamics are primarily governed by forces based on surface tension gradients in the melt. This result in lateral metal transport and the formation of a wide, shallow melt pool (Figure 5B). In contrast, the melt pool ratio of the single bead with preceding pre-heating is slightly lower than that of the single bead alone, indicating greater weld penetration. In this case, the numerical simulation will overestimate the weld penetration, which will affect the calculated aspect ratio. Table 4 confirms that increasing heat input leads to deeper melt zones, which reduces the melt pool aspect ratio.

Overall, the simulated weld pool geometries and corresponding melt pool ratios are in fair agreement with

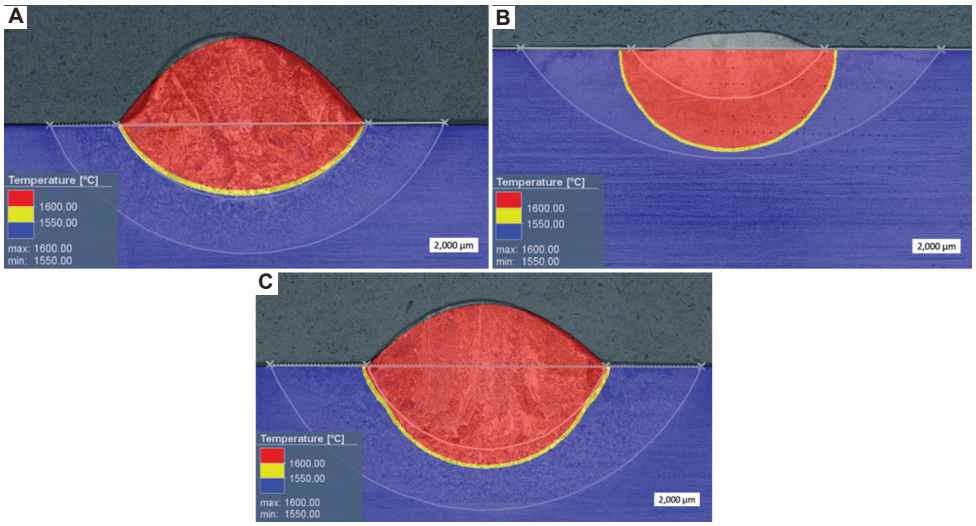

Figure 5. Comparison of calculated and experimental micrographs. (A) Single bead. (B) Pre-heating. (C) Single bead with preceding pre-heating. Scale bar: 2,000 µm

experimental observations. Recent studies, such as Liu *et al.*[33] and Bai *et al.*,[34] have shown that the inclusion of fluid flow dynamics within the melt pool can provide a more comprehensive representation of thermal and fluid behavior.

3.2.2. Thermal profiles

The thermal models are validated by comparing simulated and experimental temperature histories. Figure 6 shows the temperature evolution of single-bead deposition, pre-heating, and single-bead deposition with preceding pre-heating at each thermocouple TC1, TC2, and TC3. Depending on the distance from the heat source, different temperature–time curves are obtained.

For single bead deposition (Figure 6A), the temperature peaks decrease with increasing distance from the weld path, confirming the expected spatial thermal gradients. Once the peak temperature is reached, the heat source moves along its designated path, initiating the cooling phase. Cooling rates are inversely proportional to the distance from the heat source, with temperature profiles flattening as heat dissipation progresses. These observations are consistent with recent experimental and computational studies on WAAM thermal modeling.[16,35]

In particular, the simulated and experimental heating and cooling rates are in good agreement, confirming the accuracy of the FE framework. However, the peak temperatures predicted by the model are slightly higher than the experimental measurements. A possible explanation for this deviation is the measurement lag due to the thermocouple response time (0.9 s) and data acquisition frequency (1 s), which limits the ability of the measurement system to accurately capture rapid thermal transients, especially when the heat source passes through the thermocouple locations. Similar challenges were reported by Aarbogh *et al.*,[16] who observed peak

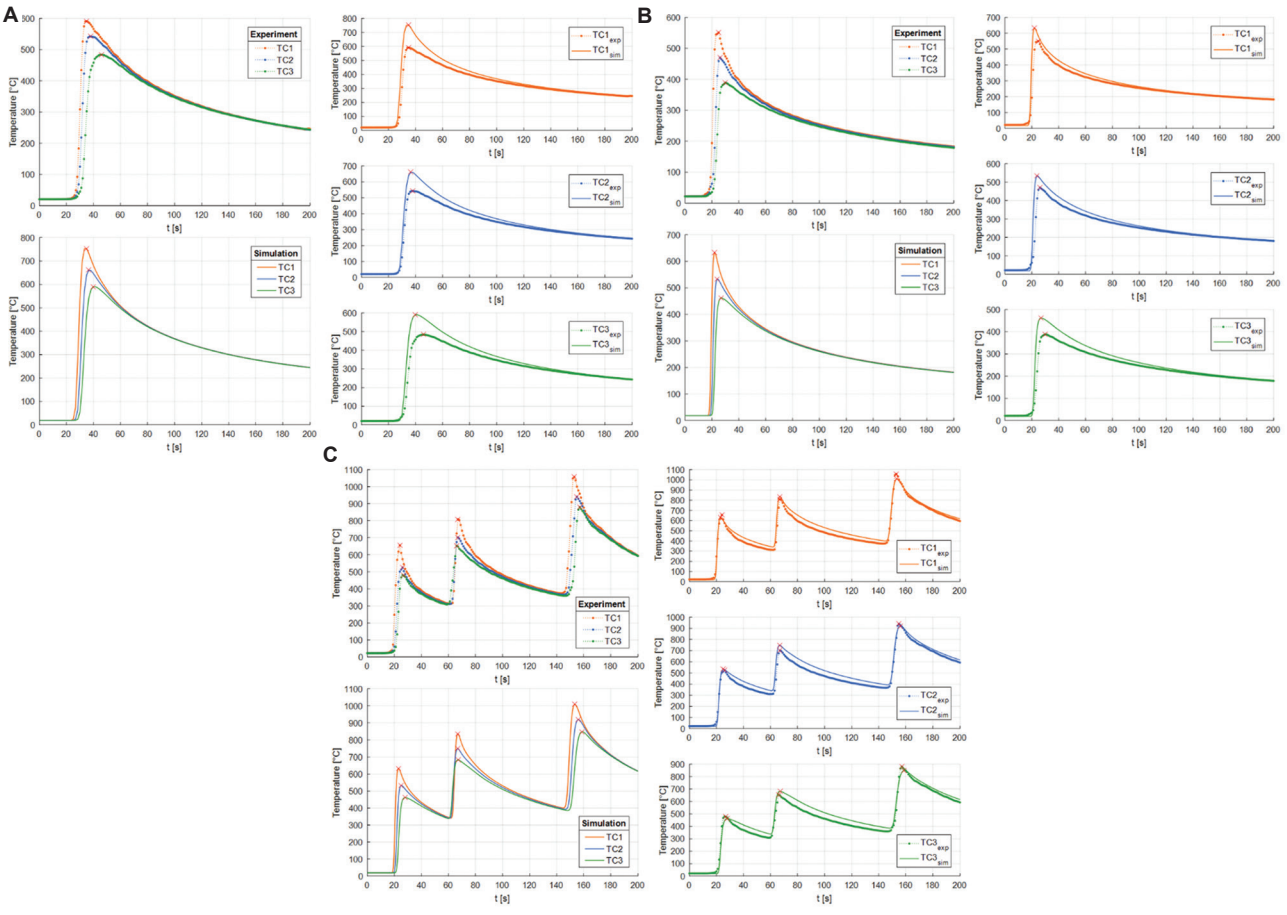

Figure 6. Overview and comparison of experimental (dotted line) and simulated (solid line) temperature profiles at various thermocouple locations obtained during (A) single bead deposition, (B) pre-heating, and (C) single bead deposition plus pre-heating. Thermocouples (TC) were positioned at pre-defined lateral and longitudinal distances relative to the weld track to capture the transient thermal behavior during deposition. Specifically, TC1 was placed at 8 mm, TC2 at 9 mm, and TC3 at 10 mm laterally from the weld centerline. In the welding direction, the thermocouples TC1 to TC3 have an offset of 5 mm.

Table 4. Melt pool ratio

Case	Preheating	Single bead	Single bead+pre-heating
Experiment	4.06	3.31	3.03
Simulation	2.22	3.67	2.45

temperature overestimation in WAAM simulations due to thermocouple placement and data acquisition limitations.

For pre-heating (Figure 6B), lower energy input per unit of length resulted in more moderate temperature peaks. Again, the peak temperatures are overestimated by the simulation, but the cooling behavior of the simulation matches the experimental trends within 100 s of reaching the peak temperatures, confirming the thermal boundary conditions used.

Figure 6C shows the thermal response for single bead deposition with pre-heating, where the simulated and experimental profiles are in good agreement. The pre-heating pass raises the temperature of the weld region to ~400°C, reducing thermal gradients and enabling stable fusion at the weld interface. The highest measured peak temperature at TC1 (~1,000°C) exceeds the β-transus temperature of Ti6Al4V, resulting in microstructural transformation, particularly within the HAZ. In a single weld bead, the final HAZ occurs at the location where the peak temperature rise is approximately equal to the β-transus temperature.[36] This was confirmed by microstructural analysis, where the HAZ half-width of 8.8 mm closely matched the location of TC1 (8 mm from the centerline). The relationship between temperature history and phase transformation is critical in Ti6Al4V processing.[11,37,38]

4. Discussion

4.1. Heat source calibration

In structural welding simulations, an accurate representation of the heat source is paramount. The shape and the heat flux distribution of the heat source must be calibrated against experimental measurements, since the heat source is as a boundary condition rather than a result of the simulation. Accurate heat source definition is essential for reliable simulation results.[18]

Table 5 shows the deviations between measured and simulated fusion zone parameters. The largest deviations occur during pre-heating, with deviations of up to 26% in width and 42% in depth. In contrast, the weld pool shape of the single bead closely matches the experimental measurements. The calculated fusion zone for the single bead with pre-heating matches well in width but deviates by up to 28% in depth. This deviation is primarily attributed to the overestimated depth of the pre-heating pass, which significantly influences the results.

The trial-and-error approach used in this study, which was also used by Aarbogh *et al.*,[16] involves iterative tuning of input parameters to fit experimental data. While common, this method is time-consuming, computationally intensive, and requires considerable expertise. To address these challenges, Gu *et al.*[18] proposed a technique to extract weld pool shape parameters directly from simulations. However, this technique primarily calculates the depth and width, with the length of the front and rear ellipsoids estimated as multiples of the measured width ($a_f = 0.5W_m$ and $a_r = 2W_m$). Aarbogh *et al.*[16] estimated the front and rear ellipsoid lengths with $a_f = W/2$ and $a_r = W$. Unlike width and depth, which can be determined directly from micrographs of the weld cross section, the exact determination of the length of the front and rear ellipsoid is more difficult to determine experimentally and are, thus, often approximated by equations. Chujutalli *et al.*[39] concluded that the parameters of the heat source influence the weld bead size collectively rather than independently.

The numerical model developed in this study for simulating the thermo-mechanical behavior of single-track deposits is distinguished by its use of a fully transient Goldak double-ellipsoid heat source formulation calibrated directly against experimental thermal profiles and melt pool geometries. This contrasts with other modeling strategies presented in the literature that focus on computational efficiency and parametric generalization. Yang *et al.*[40] proposed a semi-analytical model with temporal acceleration to efficiently simulate residual stress and deformation by accelerating heat source movement and adjusting diffusion time, which allowed significant reductions in simulation time while preserving predictive accuracy for large-scale WAAM parts. Strobl *et al.*[41] employed reduced order modeling using proper generalized decomposition to enable fast calibration and parameter estimation through efficient representation of temperature evolution in bead-on-plate welds. This method lays the groundwork for a future digital twin architecture to support real-time process control in WAAM. In contrast, Wang *et al.*[42] developed a purely geometric model for directed energy deposition based on the in-order stacking of primitives. This model approximates the buildup of deposition geometry by stacking idealized bead segments defined by simple mathematical rules. While highly efficient computationally, the model does not simulate heat transfer or mechanical responses, and instead is tailored for rapid predictions of deposition shape and volume, particularly useful for path planning and early-stage process evaluation. Recent studies have highlighted the importance of dynamic

Table 5. Heat source parameters determined by measurement and simulation

Process	Measured values (mm)			Calculated values (mm)			Relative error (%)		
	$2b_{exp}$	d_{exp}	φ_{exp}	$2b_{sim}$	d_{sim}	φ_{sim}	e_r^{2b}	e_r^{d}	e_r^{ϕ}
Preheating	6.34	1.56	4.06	8.00	3.60	2.22	26.18	42.31	-45.32
Single bead	8.88	2.68	3.31	8.80	2.4	3.67	-0.90	-10.45	10.88
Single bead+pre-heating	9.45	3.12	3.03	9.8	4.0	2.45	3.70	28.21	-19.14

Table 6. Computational time comparison between different models

Model	Adaptive mesh refinement	Parallelization	Computational time (h)
Calibration pre-heating	Yes	Yes	~ 1
Calibration single bead	Yes	Yes	~ 4
Calibration single bead+pre-heating	No	Yes	~ 2

calibration techniques for heat source modeling in WAAM. To improve heat source accuracy, in-process measurements, such as high-speed camera monitoring of the weld pool shape, can be incorporated into the calibration procedure.[34] A study by Guo *et al.*[43] introduced a convolutional neural network-based method to identify heat source parameters from the cross-sectional profile of the weld zone, providing a novel approach to heat source calibration. Ilani and Banad[44] presented a data-driven computational approach using Goldak's semi-ellipsoidal heat source model to predict melt pool geometry in metal AM.

This comparative discussion underscores that while reduced-order, semi-analytical, and geometric models provide advantages in computational efficiency or design utility, the present study contributes a robust, experimentally validated framework capable of supporting in-depth analysis of process-induced thermal and structural phenomena in WAAM.

Structural welding simulations are invaluable for predicting and optimizing geometric deviations and accumulated residual stresses before experimentation. Depending on the complexity of the models, simulation times can vary significantly, ranging from a few minutes to several days.[8,45] A comparison of the computational times used for the models is presented in Table 6. Simulations were performed on an eight-core 3.30 GHz i75820K processor with 32 GB of installed random access memory. All models have been computed using parallelization, that is, the computation of a simulation is done in parallel using multiple central processing unit cores.[46]

4.2. Thermal boundary conditions

In this study, the thermal boundary conditions, namely, emissivity ε, convective heat transfer coefficient h_c, and contact heat transfer coefficient a, were assumed to be temperature-independent. This simplification is adopted to reduce both experimental effort and computational complexity. However, it introduces inherent limitations that can affect the accuracy of the thermal model. In practice, these parameters exhibit strong temperature dependence and are affected by the dynamic nature of the heat transfer during the WAAM process. Accurately characterizing their variation over a broad temperature range requires detailed, process-representative measurements, which are often challenging to obtain experimentally. By assuming these parameters as temperature-independent, this simplification can result in localized discrepancies in the predicted temperature fields, particularly in regions with steep thermal gradients or changing surface conditions. Given the wide temperature range inherent in welding and the plasma-based WAAM process, incorporating temperature-dependent boundary conditions becomes essential for enhancing model accuracy. Future work should consider integrating such formulations. As demonstrated by Tröger *et al.*,[47] the inclusion of temperature-dependent boundary conditions significantly improves the reliability of numerical predictions in WAAM simulations.

4.3. Multi-layer welding

While the present study focuses on single-track deposition in plasma-based WAAM, understanding how these conditions evolve in multi-layer builds is essential. In multi-layer WAAM processes, previously deposited layers are subsequently remelted and reheated during the deposition of each new layer, resulting in complex thermal cycles that strongly influence both the material's microstructure and macrostructure. The macrostructure and microstructure are key determinants of the mechanical properties of WAAM-produced components.[48] Understanding these remelting effects is crucial when extrapolating single-bead observations to multi-track, multi-layer components. The evolution of the melt pool geometry, thermal gradients, and cooling rates across successive layers plays a decisive

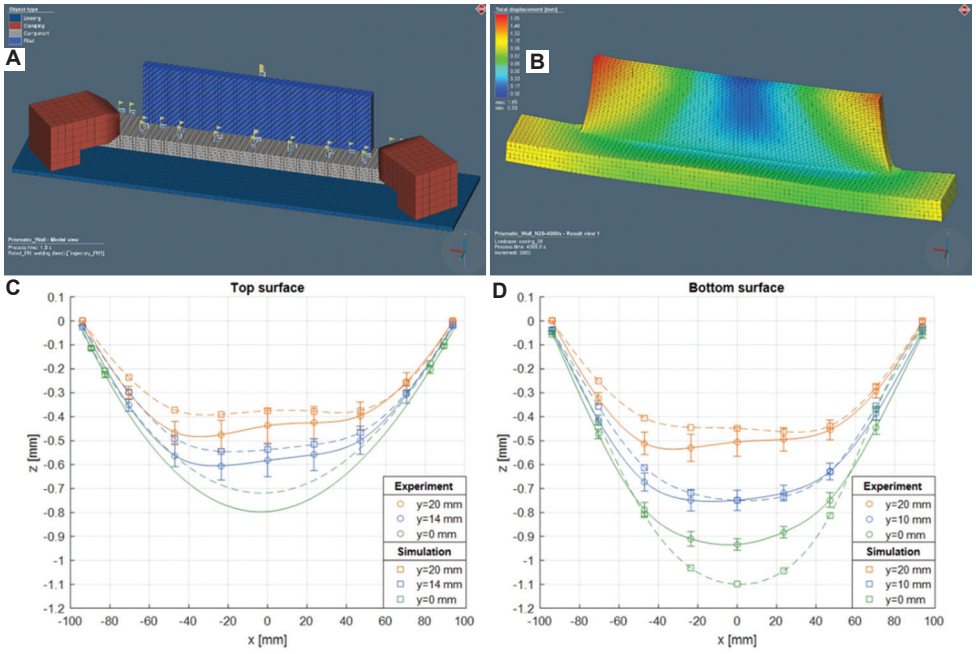

Figure 7. Plasma-based wire arc additive manufacturing simulation and mechanical behavior of a Ti-6Al-4V single-walled structure. (A) Numerical model of the single wall structure. (B) Total displacement of the wall after cooling and unclamping the top surface. (C) Top surface out-of-plane distortion along the longitudinal direction. (D) Bottom surface out-of-plane distortion along the longitudinal direction[49].

role in defining the final part's structural integrity and performance.

To evaluate the applicability of the calibrated single-bead model to more realistic build scenarios, Bielik *et al.*[49] extended the numerical simulation framework to a multi-layer deposition scenario, representative of realistic WAAM components. The thermal model was adapted to simulate the deposition process and to predict the distortion fields for a complete wall structure using Simufact Welding, as shown in Figure 7.[49] The previously derived and calibrated heat source parameters and thermal coefficients remain unchanged, with only the deposition trajectory modified to reflect the multi-pass nature of the wall geometry.

Further studies are needed to assess the correlation between the thermal and geometric evolution of the WAAM parts during multi-layer deposition (aerospace structures,[49] cylindrical, and nonlinear structures[50]). In addition, there is an increasing shift toward material deposition along arbitrary paths, enabling the modeling and fabrication of complex metal structures with greater precision and predictability.

5. Conclusion

This study presents a comprehensive methodology for calibrating the Goldak double-ellipsoid heat source model in plasma-based WAAM of Ti6Al4V single-track welds, integrating FE simulations and experimental validation. A numerical model using Simufact Welding 8.0 was developed to predict the thermal behavior of weld beads, and experimental data were used for model verification and heat source calibration. The results contribute to the optimization of structural welding simulations and the improvement of predictive modeling in AM. The main conclusions of this study are as follows:

(i) The Goldak double-ellipsoid heat source model effectively represents the experimentally determined conditions, demonstrating its suitability for structural welding simulations. However, improved temperature measurement techniques, including shielded thermocouples, advanced mounting methods, higher-frequency data logging, real-time weld pool monitoring, and data-driven algorithms, are required to improve calibration accuracy.

(ii) The simulation results successfully reproduce the temperature distributions, with predictions of the melt zone and HAZ in close agreement with experimental measurements. However, discrepancies arise due to uncertainties in heat source calibration, simplifications in bead geometry modeling, and assumptions in boundary conditions, highlighting the need for further refinement.

(iii) The effectiveness of the trial-and-error method depends on the expertise of the user, which introduces variability in results. This approach to parameter tuning is case-specific and requires recalibration for

different welding conditions, making it inefficient and resource-intensive. Future research should explore data-driven approaches, such as machine learning, regression analysis, or optimization algorithms, to improve calibration efficiency and prediction accuracy.

(iv) Assuming temperature-independent thermal boundary conditions throughout the welding process introduces potential inaccuracies. These parameters are not only temperature-dependent but also influenced by building height and geometry, requiring adaptive calibration approaches to improve model accuracy.

(v) Melt pool dynamics are not explicitly modeled in the present simulation framework, limiting the ability to capture fluid flow effects, temperature gradients, and solidification phenomena. Oversimplified thermal models can misrepresent cooling rates, affecting the microstructure evolution and mechanical properties of the deposited material. Future work should integrate computational fluid dynamics with FE simulations to improve the accuracy of weld pool dynamics, solidification modeling, and heat transfer predictions.

(vi) The results of this study can be extended to multi-pass welding simulations to facilitate the prediction of residual stresses, distortion fields, and thermal cycles in complex AM components. Coupled thermo-mechanical simulations can optimize toolpath strategies and welding parameters, reducing the need for extensive experimental testing. Model enhancements can be tested, and different numerical approaches can be compared to improve computational efficiency and result accuracy.

Acknowledgments

The authors acknowledge TU Wien Bibliothek for financial support through its Open Access Funding Programme.

Funding

Not applicable

Conflict of interest

The authors declare they have no competing interests.

Author contributions

Conceptualization: Martin Bielik, Erich Neubauer, and Ernst Kozeschnik
Investigation: Martin Bielik
Methodology: Martin Bielik
Resources: Erich Neubauer, Michael Kitzmantel, Ingo Neubauer, and Ernst Kozeschnik
Writing – original draft: Martin Bielik
Writing – review and editing: Martin Bielik and Ernst Kozeschnik

Ethics approval and consent to participate

Not applicable.

Consent for publication

Not applicable.

Availability of data

Data will be made available from the corresponding author upon reasonable request.

Further disclosure

The paper is based on the thesis of the first author, Martin Bielik. (https://repositum.tuwien.at/handle/20.500.12708/15047).

References

1. DIN EN ISO/ASTM 52900:2022-03. *Additive Fertigung-Grundlagen-Terminologie Additive Manufacturing-General Principles-Fundamentals and Vocabulary (ISO/ASTM 52900:2021)*; 2022.

   doi: 10.31030/3290011

2. Bielik M. *Thermo-Mechanical Analysis of Plasma-Based Additive Manufacturing of Ti-6Al-4V Components Using Simufact Welding. Master's Thesis*. TU Wien; 2020.

   Available from: https://repositum.tuwien.at/handle/20.500.12708/15047 [Last accessed 2025 Mar 30].

3. Bielik M, Meuthen J, Ariza-Galvan E, *et al. Plasma Metal Deposition in Aerospace Applications Enabling a Cost-Efficient Technology for High Tech Industries. Metal Additive Manufacturing Conference (MAMC), Vienna*; 2020.

4. Wallis C, Neubauer E, Kitzmantel M, *et al.* Investigations of plasma metal deposition (PMD) of 6061 and 7075 aluminum alloys for aerospace and automotive applications. *BHM Berg Hüttenmänn Monats*. 2023;168(5):209-218.

   doi: 10.1007/s00501-023-01345-4

5. Li JZ, Alkahari MR, Rosli NA, Hasan R, Sudin MN, Ramli FR. Review of wire arc additive manufacturing for 3D metal printing. *Int J Autom Technol*. 2019;13(3):346-353.

   doi: 10.20965/ijat.2019.p0346

6. Gierth M, Henckell P, Ali Y, Scholl J, Bergmann JP. Wire arc additive manufacturing (WAAM) of aluminum alloy AlMg5Mn with energy-reduced gas metal arc welding (GMAW). *Materials*. 2020;13(12):2671.

   doi: 10.3390/ma13122671

7. Masubuchi K. Residual stresses and distortion in welds. In: *Encyclopedia of Materials: Science and Technology*. Netherlands: Elsevier; 2005. p. 1-6.

   doi: 10.1016/B0-08-043152-6/01457-1

8. Ding J, Colegrove P, Mehnen J, *et al.* Thermo-mechanical analysis of wire and arc additive layer manufacturing process on large multi-layer parts. *Comput Mater Sci.* 2011;50:3315-3322.

   doi: 10.1016/j.commatsci.2011.06.023

9. Colegrove PA, Coules HE, Fairman J, *et al.* Microstructure and residual stress improvement in wire and arc additively manufactured parts through high-pressure rolling. *J Mater Process Technol*. 2013;213(10):1782-1791.

   doi: 10.1016/j.jmatprotec.2013.04.012

10. Hoye N, Li HJ, Cuiuri D, Paradowska AM. Measurement of residual stresses in titanium aerospace components formed via additive manufacturing. *Mater Sci Forum*. 2014;777:124-129.

    doi: 10.4028/www.scientific.net/MSF.777.124

11. Martina F, Roy MJ, Szost BA, *et al.* Residual stress of as-deposited and rolled wire+arc additive manufacturing Ti-6Al-4V components. *Mater Sci Technol.* 2016;32(14):1439-1448.

    doi: 10.1080/02670836.2016.1142704

12. Coules HE. Contemporary approaches to reducing weld induced residual stress. *Mater Sci Technol*. 2013;29(1):4-18.

    doi: 10.1179/1743284712Y.0000000106

13. Hu X, Chiu LN, Huang A, Liu M, Yan W. Application of melt pool profiles for parameter calibration of Goldak's heat source model. *Addit Manuf*. 2024;92:104379.

    doi: 10.1016/j.addma.2024.104379

14. Bayat M, Dong W, Thorborg J, To AC, Hattel JH. A review of multi-scale and multi-physics simulations of metal additive manufacturing processes with focus on modeling strategies. *Addit Manuf*. 2021;47:102278.

    doi: 10.1016/j.addma.2021.102278

15. Deng D, Murakawa H. Numerical simulation of temperature field and residual stress in multi-pass welds in stainless steel pipe and comparison with experimental measurements. *Comput Mater Sci*. 2006;37(3):269-277.

    doi: 10.1016/j.commatsci.2005.07.007

16. Aarbogh HM, Hamide M, Fjær HG, Mo A, Bellet M. Experimental validation of finite element codes for welding deformations. *J Mater Process Technol.* 2010;210(13):1681-1689.

    doi: 10.1016/j.jmatprotec.2010.05.014

17. Karkhin VA, Pittner A, Schwenk C, Rethmeier M. Simulation of inverse heat conduction problems in fusion welding with extended analytical heat source models. *Front Mater Sci*. 2011;5(2):119-125.

    doi: 10.1007/s11706-011-0137-1

18. Gu Y, Li YD, Yong Y, Xu FL, Su LF. Determination of parameters of double-ellipsoidal heat source model based on optimization method. *Weld World*. 2019;63(2):365-376.

    doi: 10.1007/s40194-018-00678-w

19. Goldak J, Chakravarti A, Bibby M. A new finite element model for welding heat sources. *Metall Trans B*. 1984;15(2):299-305.

    doi: 10.1007/BF02667333

20. *Simufact. Infosheet Heat Source. Simufact Welding Tutorial.* Hamburg, Germany: Simufact Engineering GmbH; 2018.

21. Lundbäck A. *Modelling of Weld Path for Use in Simulations. Master's Thesis*. Sweden: Lulea University of Technology; 2000.

22. Fachinotti VD, Anca AA, Cardona A. Analytical solutions of the thermal field induced by moving double-ellipsoidal and double-elliptical heat sources in a semi-infinite body. *Int J Numer Methods Biomed Eng*. 2011;27(4):595-607.

    doi: 10.1002/cnm.1324

23. Megahed M, Mindt HW, N'Dri N, Duan H, Desmaison O. Metal additive-manufacturing process and residual stress modeling. *Integr Mater Manuf Innov*. 2016;5(1):61-93.

    doi: 10.1186/s40192-016-0047-2

24. Radaj D. *Wärmewirkungen Des Schweißens [Thermal Effects of Welding]*. Berlin, Heidelberg: Springer; 1988.

    doi: 10.1007/978-3-642-52297-0

25. *Simufact. Infosheet Boundary Conditions Thermal.* Simufact Welding Tutorial. Hamburg, Germany: Simufact Engineering GmbH; 2018.

26. Helbig P. *Kalibrierung Von Ersatzwärmequellen Für Die numerische Simulation von Laserschweißprozessen [Calibration of Representative Heat Sources for the Numerical Simulation of Laser Welding Processes]. Master's Thesis.* Kassel: Universität Kassel; 2018.

27. Xiong J, Lei Y, Li R. Finite element analysis and experimental validation of thermal behavior for thin-walled parts in GMAW-based additive manufacturing with various substrate preheating temperatures. *Appl Therm Eng.* 2017;126:43-52.

    doi: 10.1016/j.applthermaleng.2017.07.168

28. Wang J, Lin X, Wang J, *et al.* Grain morphology evolution and texture characterization of wire and arc additive manufactured Ti-6Al-4V. *J Alloys Compd*. 2018;768:97-113.

    doi: 10.1016/j.jallcom.2018.07.235

29. Abe T, Kaneko J, Sasahara H. Thermal sensing and heat input control for thin-walled structure building based on numerical simulation for wire and arc additive manufacturing. *Addit Manuf*. 2020;35:101357.

    doi: 10.1016/j.addma.2020.101357

30. Sampaio RFV, Pragana JPM, Bragança IMF, Silva CMA, Nielsen CV, Martins PAF. Modelling of wire-arc additive manufacturing a review. *Adv Ind Manuf Eng*. 2023;6:100121.

doi: 10.1016/j.aime.2023.100121

31. Deyev G, Deyev D. *Surface Phenomena in Fusion Welding Processes*. 1st ed. United States: CRC Press; 2005.

doi: 10.1201/9781420036299

32. Ou W, Knapp GL, Mukherjee T, Wei Y, DebRoy T. An improved heat transfer and fluid flow model of wire-arc additive manufacturing. *Int J Heat Mass Transf*. 2021;167:120835.

doi: 10.1016/j.ijheatmasstransfer.2020.120835

33. Liu C, Wu Y, Zhou J, Wen Y, Wang L, Xie L. Effect of in situ electromagnetic field manipulation on the microstructure and hardness of titanium alloy during laser melting deposition. *Mater Sci Addit Manuf*. 2025;4(1):8332.

doi: 10.36922/msam.8332

34. Bai X, Colegrove P, Ding J, *et al.* Numerical analysis of heat transfer and fluid flow in multilayer deposition of PAW-based wire and arc additive manufacturing. *Int J Heat Mass Transf*. 2018;124:504-516.

doi: 10.1016/j.ijheatmasstransfer.2018.03.085

35. Belhadj M, Werda S, Belhadj A, Kromer R, Darnis P. *Thermal Analysis of Wire Arc Additive Manufacturing Process*. *ESAFORM 2021*; 2021.

doi: 10.25518/esaform21.4095

36. Liu S, Shin YC. Additive manufacturing of Ti6Al4V alloy: A review. *Mater Des*. 2019;164:107552.

doi: 10.1016/j.matdes.2018.107552

37. Wu B, Pan Z, Ding D, Cuiuri D, Li H. Effects of heat accumulation on microstructure and mechanical properties of Ti6Al4V alloy deposited by wire arc additive manufacturing. *Addit Manuf*. 2018;23:151-160.

doi: 10.1016/j.addma.2018.08.004

38. Hönnige J, Colegrove P, Prangnell P, Ho A, Williams S. The effect of thermal history on microstructural evolution, cold-work refinement and α/β growth in Ti-6Al-4V wire + Arc AM. *Appl Phys [ArXiv Preprint]*; 2018.

doi: 10.48550/ARXIV.1811.02903

39. Chujutalli JH, Lourenço MI, Estefen SF. Experimental-based methodology for the double ellipsoidal heat source parameters in welding simulations. *Mar Syst Ocean Technol*. 2020;15(2):110-123.

doi: 10.1007/s40868-020-00074-4

40. Yang Y, Lin H, Li Q. A computationally efficient thermo-mechanical model with temporal acceleration for prediction of residual stresses and deformations in WAAM. *Virtual Phys Prototyp*. 2024;19(1):e2349683.

doi: 10.1080/17452759.2024.2349683

41. Strobl D, Unger JF, Ghnatios C, *et al.* Efficient bead-on-plate weld model for parameter estimation towards effective wire arc additive manufacturing simulation. *Weld World*. 2024;68(4):969-986.

doi: 10.1007/s40194-024-01700-0

42. Wang X, Meng D, Yi H, Yan Z, Xiao J, Chen S. A novel model for directed energy deposition-arc based on in-order stacking of primitives. *Virtual Phys Prototyp*. 2024;19(1):e2291471.

doi: 10.1080/17452759.2023.2291471

43. Guo Z, Jiang H, He L, Lei Z, Bai R. CNN-empowered identification of heat source parameters from the cross-section profile of laser-welded zone. *Int J Adv Manuf Technol*. 2024;130(11-12):5441-5455.

doi: 10.1007/s00170-024-13054-4

44. Ilani MA, Banad YM. Modeling Melt Pool Geometry in Metal Additive Manufacturing Using Goldak's Semi-Ellipsoidal Heat Source: A Data-Driven Computational Approach. *Numer Anal [ArXiv Preprint]*; 2024.

doi: 10.48550/ARXIV.2404.08834

45. Martukanitz R, Michaleris P, Palmer T, *et al.* Toward an integrated computational system for describing the additive manufacturing process for metallic materials. *Addit Manuf*. 2014;1-4:52-63.

doi: 10.1016/j.addma.2014.09.002

46. *Simufact Infosheet Parallelization*. Simufact Welding Tutorial; 2018.

47. Tröger JA, Hartmann S, Treutler K, Potschka A, Wesling V. Simulation-based process parameter optimization for wire arc additive manufacturing. *Prog Addit Manuf*. 2025;10(1):1-14.

doi: 10.1007/s40964-024-00597-x

48. Wang F, Williams S, Colegrove P, Antonysamy AA. Microstructure and mechanical properties of wire and arc additive manufactured Ti-6Al-4V. *Metall Mater Trans A*. 2013;44(2):968-977.

doi: 10.1007/s11661-012-1444-6

49. Bielik M, Neubauer E, Kitzmantel M, Neubauer I, Kozeschnik E. A simulation approach for series production of plasma-based additive manufacturing of Ti-6Al-4V components. *Math Model Weld Phenomena*. 2022;13:361-393.

doi: 10.3217/978-3-85125-968-1-20

50. Graf M, Hälsig A, Höfer K, Awiszus B, Mayr P. Thermo-mechanical modelling of wire-arc additive manufacturing (WAAM) of semi-finished products. *Metals*. 2018;8(12):1009.

doi: 10.3390/met8121009